

Manuscript version: Author's Accepted Manuscript

The version presented in WRAP is the author's accepted manuscript and may differ from the published version or Version of Record.

Persistent WRAP URL:

<http://wrap.warwick.ac.uk/146814>

How to cite:

Please refer to published version for the most recent bibliographic citation information. If a published version is known of, the repository item page linked to above, will contain details on accessing it.

Copyright and reuse:

The Warwick Research Archive Portal (WRAP) makes this work by researchers of the University of Warwick available open access under the following conditions.

© 2020 Elsevier. Licensed under the Creative Commons Attribution-NonCommercial-NoDerivatives 4.0 International <http://creativecommons.org/licenses/by-nc-nd/4.0/>.



Publisher's statement:

Please refer to the repository item page, publisher's statement section, for further information.

For more information, please contact the WRAP Team at: wrap@warwick.ac.uk.

Three-point flexural performance of tailor-braided thermoplastic composite beam structures

Anubhav Singh^{a,*}, Neil Reynolds^a, Elspeth M Keating^a, Alastair E Barnett^b, Steve K Barbour^b, Darren J Hughes^a

^a WMG, University of Warwick, Coventry CV4 7AL, United Kingdom

^b Composite Braiding Limited, Derby DE24 9FU, United Kingdom

*Corresponding author, E-mail: A.Singh.10@warwick.ac.uk

<https://doi.org/10.1016/j.compstruct.2020.113521>

Abstract

This work investigates the potential of improving the mechanical performance of braided composite beams through the introduction of local braid angle variations. Tubular braided beams with a 45°/60°/45° length-wise (axial) braid angle variation were manufactured and tested in quasi-static three-point flexure and their performance was compared with beams having a layer-wise (radial) [$\pm 60^\circ/\pm 45^\circ/\pm 45^\circ$] variation. Compared to beams having uniform braid angles, axial braid angle tailoring resulted in equivalent flexural performance with a 24% reduction in part weight. In contrast, tailoring in the radial direction did not yield any improvement in mass-specific performance. Deformation analysis of the beams using an extensometer and digital image correlation showed that an axial braid angle variation in each layer resulted in a comprehensive shift in deformation characteristics. Changing the braid angle in the outer layer across the whole beam showed partial change in deformation mode, but did not match the modification observed through axial variation.

Keywords: Braiding; Tailoring; Thermoplastic; Flexure; Lightweighting; Digital image correlation

Introduction

Braiding has emerged as an attractive composite manufacturing technology over the last few decades. The technique uses automated braiding machines to produce multi-layered dry fibre preforms through controlled interlacing of the fibres over the surface of a mandrel. The process is inherently flexible in terms of shape, size and orientation of the mandrels and hence creates near-net shape preforms [1]. Consequently, the preforms require minimal trimming operations and hence reduce material waste. Additionally, the complex fibre interlacings, achieved through the braiding process, impart superior mechanical performance under certain load cases compared to competitor manufacturing processes. These advantages of braided composites have led to their adoption for the production of load-bearing structures in the automotive and aerospace industry [2].

A particular advantage of composite materials is the possibility of modifying them as per the bespoke requirements of a given application. Such modifications are largely embodied in components via judicious variation of fibre orientation and part thickness [3,4]. Braided composites are no exception, and braiding provides several avenues to modify part performance to a structure's local specific requirements. For instance, the mechanical properties of a braided structure can be enhanced in the length-wise direction by the selective introduction of axial tows [5]. Additionally, the process can readily combine different types of reinforcement without adding significant time or cost. For instance, braiding of carbon and aramid tows was demonstrated to enhance mechanical stiffness as well as energy absorption [5]. A potential technique for modification of braided

composites is through the variation of braid angle in different regions of the composite. The braid angle influences the material characteristics as well as the thickness of a braided composite [6–14]. Therefore, local variations in braid angle provide significant potential for improvement in overall structural performance. This inherent capability of the braiding process has been utilised in the past to produce braided components with varying properties. Carey et al. [15] varied the braid angle for achieving variable stiffness along the length of composite catheter shafts with different combinations of fibres and matrices. Similarly, variable stiffness was achieved by Fujihara et al. [16] in dental posts by braiding the fibres with a graded variation in braid angle. Boss et al. [17] fabricated braided rods with a gradual braid angle variation. The flexural and tensile moduli of the rods were found to be an average of the properties corresponding to beams with uniform braid angles, while the overall tensile strength depended on the braid angle region that had the lowest strength. Ganesh et al. [18] used braided preforms with graded braiding angles in single-bond lap joints to gradually reduce the longitudinal modulus from the loaded end to the joint's overlap region. The results showed a more uniform stress distribution in the overlap area. Stanier et al. [19,20] performed open-hole tensile tests on triaxially braided rectangular plates with a controlled braid angle variation and reported an improvement in strength as compared to beams with a constant braid angle. Similar improvement was observed by Huang et al. [21] in the tensile strength of braided tubes with graded braid angle profiles.

The abovementioned studies showed that braid angle variations can result in improved performance. However, the available studies are limited to uniaxial loads. In order to establish the viability of braided composites with variable braid angle, it is important to analyse their performance in other structural load cases. A simple and effective loading scenario for global assessment of structural performance is provided by a three-point flexure test. The localised loading in three-point flexure subjects the test specimen to variable stress states and mixed-mode failure, thus making it ideal for testing beam structures where trade-offs between different characteristics that depend on braid angle can be studied. Moreover, there are several previous studies that present three-point flexure as a means to explore the performance of beam structures with variable properties along the axis. Duan et al. [22] tested what they termed 'tailor-rolled' top hat metallic structures with preferentially greater thickness in the loading zone. Similarly, Sun et al. [23] tested thickness-graded metallic beams under flexure. Both of these approaches were reported to achieve significant weight saving without compromising mechanical performance. In addition to variable property metallic beams, the results reported by Keating [24] and Sun et al. [25] showed lightweighting benefits are also achievable by locally reinforcing metallic beams with composite patches in the loading region of a three-point flexure test. As the weight of a braided beam is directly related to the braid angle [5], controlled braid angle variations also presents an opportunity for structural lightweighting as reported for metallic and hybrid structures.

Recent work performed by the authors studied the effect of braid angle on three-point flexural performance of uni-braided (UBr) thermoplastic composite beams, i.e. beams with a constant braid angle [26]. Building on this recent work, the authors propose a 'tailor-braiding' approach for a composite braided structure in order to create structurally efficient components offering performance improvement over UBr variants. This current study uses the results obtained from testing UBr beams to devise suitable strategies for length-wise tailoring of braid angle, i.e. axial tailor-braiding (TBr_A), followed by manufacturing and testing of the TBr_A beams in static three-point flexure. Results reported by Wu et al. [27] had previously shown that a radial variation can modify the flexural

response. Therefore, beams with a layer-wise braid angle variation, i.e. radial tailor-braiding (TBr_R) are also manufactured and tested for comparison. Using three-point flexure as a test scenario, the results are presented and analysed against those obtained from the previous UBr beams to determine the potential of the two tailor-braiding (TBr) strategies for achieving performance improvements. Moreover, since most of the previous research on braided structures has focused on thermosetting matrix composites; given the difference in ductility between thermoset and thermoplastic polymer matrices, it is expected that the results obtained in this work will invite further research questions over the influence of the matrix in tailor-braided structures.

Three-point flexure performance of UBr beams

Previously, 420 mm-long uni-braided beams with an outer diameter of 35 mm having braid angles of 45° (UBr₄₅) and 60° (UBr₆₀) were tested in three-point flexure [26]. During the tests, the applied crosshead displacement resulted in two principal deformation modes: global beam flexure and localised crushing. Quantitatively, 45% and 19% of the total deflection in the UBr₄₅ and UBr₆₀ beams respectively was through local crushing. The stiffness (S) of the tested beams was evaluated in the displacement range between 0.2 mm and 1 mm using Equation 1. The energy absorption (E_{abs}) was also determined by evaluating the area under the load-displacement curves, as shown in Equation 2. The beams were deformed up to a crosshead displacement of 18 mm.

$$S = \frac{(P_1 - P_{0.2})}{(0.8)} \quad (1)$$

$$E_{abs} = \int_0^{18} P \, dx \quad (2)$$

where S: stiffness (N/mm); P₁: load (N) at 1 mm crosshead displacement and P_{0.2}: load (N) at 0.2 mm crosshead displacement; E_{abs}: energy absorption (Nmm); x: displacement (mm).

The three performance indices: S, peak load (P_{max}) and E_{abs} corresponding to the UBr beams during three-point flexure are shown in Figure 1. Compared to the UBr₄₅ beams, S, P_{max} and E_{abs} were 17%, 60% and 43% greater respectively for the UBr₆₀ beams, clearly demonstrating overall superior mechanical performance. Beam deformation analyses indicated that for the tested UBr beams, resistance to localised crush was the critical governing factor in overall mechanical performance.

In addition to the mechanical performance indices reported in [26], Figure 1 also shows the measured mass values for the two UBr beam types, which are presented for the first time in this work. Comparing the average masses revealed that the relative improvement in mechanical performance of the UBr₆₀ beams was accompanied with a 44% increase in mass as compared to the UBr₄₅ beams. This data is used to calculate mass-normalised performance indices (S', P'_{max}, E'_{abs}), and these are also shown in Figure 1. In order to compare the mass-specific properties, a single factor analysis of variance (ANOVA) was performed. A significance level of 0.05 was selected and the resulting p-values are listed in Table 1.

As the p-value for the mass-specific energy absorption (E'_{abs}) was greater than 0.05, it could be stated with 95% confidence that the difference in E'_{abs} between the UBr₄₅ and UBr₆₀ beams was not statistically significant; however differences between beams in specific stiffness (S') and specific peak load (P'_{max}) were statistically significant. Specifically, S' was 23% greater for UBr₄₅ beams, while P'_{max} was 11% greater for UBr₆₀ beams.

Therefore, from a structural lightweighting perspective, the UBr₆₀ beams did not offer a clear advantage over the UBr₄₅ beams under flexural loading.

These mechanical test results as obtained from the UBr beams were used as a baseline for devising a tailor-braiding strategy for the current study. Given the UBr₆₀ beams' greater resistance to localised crush and the improved specific (flexural) stiffness of the UBr₄₅ beams, it was hypothesised that beams with a braid angle of 60° in the central loading region with adjacent regions of 45° located symmetrically either side would result in overall improved mechanical performance compared to 45° beams, whilst being significantly lighter than UBr₆₀ beams. Therefore, as shown in Figure 2, a 45°/60°/45° configuration was selected for the TBr_A beams. For the TBr_R beams, as the outer layer directly interacts with the loading roller, beams with two inner layers of 45° and an outer layer of 60°, i.e. a [±60°/±45°/±45°] braid angle profile, were manufactured for comparison with the TBr_A beams.

Experimental methodology

Materials and manufacturing

Commingle E-glass/polyamide 6 (PA6) tows were braided using a 64-carrier machine. The details of the material and braiding process are listed in Table 2.

During the braiding process, the fibre tows originate from the bobbins on the braiding machine. The bobbins are in constant circular motion in a fixed plane adjacent to the braiding machine, called the braiding plane (BP). All the fibre tows converge on the braiding mandrel in a plane known as fall plane (FP). As a consequence of the location of the FP relative to the BP, the angle subtended between a fibre tow and the mandrel is equal to the braid angle. This is schematically depicted in Figure 3.

As shown by Nishimoto et al. [28], an axial braid angle variation necessitates a shift of the FP. This creates a transition region on the resulting braided beam between the FPs of the two target braid angles that has a continuously varying braid angle. However, during the braiding of the TBr_A preforms, the transition regions were found to be extremely long with respect to the length of the beams produced and tested in this work. Therefore, a step transition was adopted. This was achieved by braiding the tows in a start/stop mode, as depicted in Figure 4(a). After braiding the required length at the FP corresponding to 45°, the process was stopped, the mandrel was moved linearly to align the tow converging point with the FP of 60° and the braiding process was restarted with the corresponding braiding parameters. This adjustment process was repeated to achieve each required length of tailored braid. The FPs for braid angles of 45° and 60° are shown in Figure 4(b). The adjustment process was repeated for each layer of these multi-layer braided preforms. On the other hand, the braiding of TBr_R preforms was conducted by braiding the two inner layers at 45° and the outermost layer with a braid angle of 60°.

Following the braiding process, the preforms having 3 layers of braided fabric were used to produce tubular braided beams with an outer diameter of 35 mm in a bladder moulding process, known as Rapid Variothermal Moulding (RVM). The entire process of preform preparation and moulding is shown step-by-step in Figure 5. For further details regarding the manufacturing process, the readers are referred to [26] and [29].

The produced TBr_A beams had an approximately 80 mm-long region of braid angle of 60° in the centre, with equal-length regions of 45° located at both ends. The outer surfaces of the TBr_A and TBr_R braided beams produced using the RVM process are shown in Figure 6. For the purpose of comparison, surfaces of UBr₄₅ and UBr₆₀ beams are also shown. The visible discolouration on beam surfaces was due to exposure of the molten PA6 polymer to ambient air during the moulding process [26]. There was an observable difference in the brownish discolouration of the UBr₄₅ and UBr₆₀ beams, which occurred due to larger air gaps between tows in the UBr₄₅ beams. For the TBr_A beams, the difference in discolouration between regions with braid angles of 45° and 60° created an identifiable transition zone between the two regions. As shown in the figure, the fibres in both the regions resemble the outer surface characteristics of the corresponding UBr beams. Fibre waviness was observed at angle transition points as well as the adjacent 60° region in all of the beams. This was likely due to the discrete step-change in braid angle during manufacturing (as opposed to a continuous variation); minimisation of this uncontrolled defect was not within the scope of the present study. On the other hand, the discolouration on the surface of the TBr_R beams was an intermediate between the UBr₄₅ and UBr₆₀ beams. Unlike the UBr as well as TBr_A beams, the TBr_R beams did not show any dry fibres on the outer surface. This is discussed later in the paper.

The mass of all the beams was measured after cutting them all to a length of 420 mm (Figure 7). The mean mass of the TBr_A beams was 3% lower than the TBr_R beams. Considering the UBr beams, the TBr beams were approximately 10% heavier than the UBr₄₅ beams, but 24% lighter than UBr₆₀ beams.

Braid angle was physically measured at randomly located points on the outer surface for 4 repeats for both types of TBr beams and are shown in Figure 8. Due to the fibre waviness at the transition points and shorter span of the 60° region in the TBr_A beams, limited measurements (minimum 6) were possible. The deviation in the measured braid angles were similar to the values previously recorded for the UBr beams.

Specimens of 10 mm length were extracted from one untested repeat each for the TBr_A and TBr_R beams. The extracted specimens were cold-mounted in epoxy resin and polished to a 3 µm finish, following which the cross section perpendicular to the beam axis was analysed using images from a macro zoom camera. The thickness of the beams was measured at a minimum of 400 locations across two polished specimens prepared for the 45° and 60° regions of the TBr_A beam as well as TBr_R beam. The measured thickness distributions are represented through box plots shown in Figure 9. The thickness of the UBr₄₅ and UBr₆₀ beams, reported in [26] are also shown for comparison. The thickness measurements of the two regions of TBr_A beam are in reasonable agreement with the corresponding UBr beams. However, the 60° region showed greater variance against its UBr counterpart as compared to the 45° region, which could be a result of excessive braid angle distortions, observable as fibre waviness on the outer surface. As expected, the thickness distribution of the TBr_R beams resided between the measured values corresponding to the two UBr beams, with the mean thickness being approximately 19% greater than UBr₄₅ but 17% less than UBr₆₀.

The polished section specimens were also imaged using a ZEISS Axio Imager 2 microscope fitted with a 5 megapixel AxioCam 305 digital camera at 5x magnification. Figures 10 (a) and (b) shows selected micrographs of the 60° and 45° regions of TBr_A beams respectively. For reference, micrographs of UBr₄₅ and UBr₆₀ beams are also shown. The TBr_A and corresponding UBr micrographs showed comparable characteristics, with fibre

tows separated by resin rich regions. Regions with extensive tow distortion/fibre waviness are highlighted in the micrograph pertaining to the 60° region of TBr_A beams. The waviness could affect the mechanical performance of the beams and highlights scope for improving process control during the tailor-braiding process. A micrograph of a TBr_R beam is shown in Figure 10(c). Notably, a resin-rich region was visible in the outermost layer (60° layer) above the fibre tows, explaining the absence of dry regions on the outer surface. The micrographs of both the TBr beams showed intra- and inter-tow voids similar to the UBr beam sections. However, based on the prior detailed analysis of void content morphology previously conducted [26] in addition to the mechanical test results of the UBr beams, it is proposed that the presence of voids does not prejudice the comparative analysis of mechanical performance as performed here.

Quasi-static three-point flexure tests

Quasi-static three-point flexural testing was performed using an Instron 5800R test machine with a 100 kN load cell in compression mode. Figure 11(a) shows the test setup used. The parameters used during the test are listed in Table 3. All parameters are consistent with those used in the previous reference study to test the UBr beams. During the tests, the vertical displacement at the beams' bottom surface was recorded using a linear deflectometer created by combining an Instron 2630-112 extensometer and a spring-loaded plunger, as shown in Figure 11(b). This was used to evaluate the localised crushing in the central loading region by subtracting the recorded value from the crosshead displacement. Six repeat tests of each beam type were conducted, while the bottom surface displacement was recorded for three repeats each. The tests were stopped at a crosshead displacement of 18 mm as significant lateral movement was observed at the beam-support roller interfaces upon deflections beyond this. Similar to the analysis performed for UBr beams, the mechanical response of the TBr beams were compared using the indices S' , P'_{\max} and E'_{abs} . The mean P'_{\max} and E'_{abs} of UBr₆₀ beams and mean S' of UBr₄₅ beams were selected as the benchmark values (being the highest in each case) against which the performance of the TBr beams would be evaluated.

During the three-point flexure tests, the surface strain distribution was evaluated using a three-dimensional digital image correlation (3D-DIC) system. These optical strain measurements were conducted for one single repeat during testing of both TBr_A and TBr_R beams. The GOM 12M system was used to capture 3D-DIC images, and GOM ARAMIS and GOM Correlate Professional were used for the acquisition and post-processing of the DIC images. For all the conducted measurements, the Region of Interest (RoI) was the region directly under the central loading roller, as deformations were concentrated in this region. The parameters of the DIC system are listed in Table 4. The surface elements created in the software from the recognised facets were realigned in the software to ensure consistent orientation of the measured displacements. In order to estimate the accuracy of the measurement system, six static (undeformed) images were recorded and analysed. The evaluated bias and resolution of the measurements are listed in Table 5.

The acquired optical strain measurements were used to compare the deformation in different regions of the beam. Figure 12(a) shows three separate line sections along which flexural strains 1, 2 and 3 are evaluated - corresponding to the top, middle and bottom regions respectively. For each line section, the flexural strain was calculated as the average of the axial strains at all integration points along the section. Similarly, Figure 12(b) shows the sections used to record the point-wise downward y-displacements y_1 , y_2 and y_3 in the top, middle and bottom regions respectively. Analysing the obtained flexural strain and y-displacements in different regions

of the beams enabled further comparison of deformation modes between the TBr variants as well as against the UBr beams. For further details of the analysis process, the readers are referred to [26].

Results and discussion

Three-point flexure performance of tailor-braided beams

Figure 13(a) shows the three-point flexure load-displacement curves corresponding to the tested TBr beams.

The behaviour of the TBr_A and TBr_R beams was similar up to a crosshead deflection of approximately 5 mm. Upon further deformation, the load borne by the TBr_R beams plateaued with frequent undulations. On the other hand, the response corresponding to the TBr_A beams showed a generally consistent increase throughout the deformation with minor inconsistency between the repeats within the last two millimetres of deflection. For the purpose of comparison, the load-displacement data of the TBr_A and TBr_R beams are shown along with the response recorded for UBr beams in Figure 13 (b) and (c) respectively. Despite the significant fibre waviness, the TBr_A and UBr₆₀ beams showed very similar load-displacement behaviour. The plateauing load trends observed for the TBr_R beams was analogous to the UBr₄₅ beams, however the magnitude of the load was greater for the TBr_R beams.

In order to identify and semi-quantitatively compare the damage in the tested beams, active infrared thermography was employed *ex-situ*. The beams were held in free space using a retort stand and heated internally using hot air (~150 °C) supplied from a heat gun for approximately 10 seconds whilst an FLIR SC5200 infrared camera was used to acquire thermal images at 25 Hz of the outer surface of the beams in the region of interest. This image acquisition was conducted for the load bearing surface (upper) as well as the opposite (lower) surface for one repeat of each beam type. The acquired images were processed using FLIR Altair thermography software, evaluating the variation in heating detected at the beam surface due to differential conduction by subtracting the reference frame (unheated surface, $t = 0$ s) from the target frame ($t = 3$ s). The differential thermal images corresponding to different beam types are shown in Figure 14. Optical images of the same upper and lower surfaces are also shown for context. The different digital levels visible in the thermal images of the beam surface represent difference in heat conduction outward through the beam wall from the inner surface that arise from variabilities in wall thickness, density (local fibre/resin content) as well as localised damage. Damaged regions in the composite such as local cracking and larger-scale delaminations present the most severe impediment to heat conduction (as compared to changes in density and wall thickness) and will therefore be clearly visible at the highest end of the differential scale. The colour scale was automatically adjusted for each image to span the maximum and minimum detected levels and therefore there is not a common scale applied to the images; however, this approach allows semi-quantitative assessment of the differential conductive heating within each discrete image. Damage is visible on the upper loading surfaces of all the tested beams in the thermal images with the lowest surface temperature visible as lightest red within each thermal image, and corresponds to the surface damage seen in the optical images, with identical location and morphology in both image types. The images indicate that the damage initiated under the loading roller followed by propagation along the braided fibres in close proximity. However, neither the optical nor thermal images revealed any damage on the lower surfaces of the beams. Interestingly, this semi-quantitative differential thermal analysis approach also clearly reveals the characteristic trellis braided tow pattern within the beams

(blue-black-white, as per differential fibre/resin density), and the inherent wall thickening at the higher 60° braid angle (darker red); this occurs in local patches along the UBr₆₀ beam and within the entire 60° mid-section of TBr_A beam.

Analysis of lightweighting benefits of tailor-braiding

Figure 15 shows the S , P_{\max} and E_{abs} as well as the mass-specific values (S' , P'_{\max} and E'_{abs}) for all of the tested beam types. As expected from the load-displacement responses, the absolute values (S , P_{\max} and E_{abs}) of each index were indistinguishable between UBr₆₀ and TBr_A beams.

Single-factor ANOVA was performed for each mass-specific property. The resulting p-values for each comparison are listed in Table 6. All the values being less than 0.05 indicate that across the four types of beams being compared, the differences between all the mass-specific properties were statistically significant.

In order to further explore these differences, a post-hoc analysis was performed using Tukey-Kramer method [30]. The Studentised range statistic q was evaluated for each pair using Equation 3.

$$q_{AB} = \frac{|\mu_A - \mu_B|}{\sqrt{\frac{MS_W}{2} \left(\frac{1}{n_A} + \frac{1}{n_B} \right)}} \quad (3)$$

where μ_A : mean for sample A; μ_B : mean for sample B; n_A : sample size of A; n_B : sample size of B and MS_W : mean square error within.

As per the method, depending on the number of samples, a critical q -value is determined from a standard q -table. If the evaluated q -value from Equation (3) is greater than the critical q -value, the difference between the means corresponding to the respective pair of samples is statistically significant. The obtained q -values corresponding to every comparison are listed in Table 7 with the critical q -values. Referring to the table yields the following observations regarding mass-normalised performance:

- (i) **TBr_A versus TBr_R**: The comparison of the two tailored beam configurations showed no significant difference in S' . However, the P'_{\max} and E'_{abs} were greater for TBr_A beams, the mean values being greater by 41% and 28% respectively.
- (ii) **TBr_A versus UBr**: There were no statistically significant differences measured between the TBr_A beams and UBr₄₅ beams with respect to S' . However, P'_{\max} and E'_{abs} were both greater for the TBr_A beams with the mean values being 45% and 31% higher. On the other hand, comparisons with the UBr₆₀ beams showed that all the performance indices were greater for the TBr_A beams, showing substantial increases in S' , P'_{\max} and E'_{abs} of 26%, 30% and 31% respectively. Therefore, the local axial tailoring (TBr_A) delivered improvements against most benchmark (UBr) performance indices.
- (iii) **TBr_R versus UBr**: There were no significant differences measured between the TBr_R and UBr₄₅ beams across all three performance indices. Similarly, comparing TBr_R beam performance against that of the UBr₆₀ beams, E'_{abs} was found to be comparable. The S' of TBr_R exceeded that of UBr₆₀ beams by 19%, while the P'_{\max} of UBr₆₀ beams was greater by 8%. Overall, braiding the outer layer at a higher braid angle did not yield significant improvements over any of the three benchmark UBr performance indices.

Analysis and comparison of beam deformation

Figure 16 shows the measured localised crushing against crosshead displacement for the tested beams. The TBr_A and UBr₆₀ beams showed matching trends, with the localised crushing accounting for approximately 17% and 19% of the total crosshead displacement for TBr_A and UBr₆₀ beams respectively. The TBr_R beam showed a reduction in localised crush with respect to the UBr₄₅ beams, with an overall localised crushing of 35% compared to 45% for the latter. However, the transitions in slope of the curves occurred at identical crosshead displacement values for both beams.

The optically-measured axial strain maps are shown for the tested beams in Figure 17. Optical strain analysis for the UBr beams, previously reported in [26], had revealed that greater localised crush resulted in a reduction in applied strains on the bottom (tensile) surface of the beam – the predominant deformation mode was local crush, thus reducing global flexure. A similar correlation between localised crush and lower surface strains is also observed in the TBr beams. Similar to observations from the UBr₆₀ beam, during the final millimetres of the applied deflection, a region showing surface strains of >1.5% developed on the lower (tensile) surface of the TBr_A beam at peak deformation, with clear regions of strain concentration corresponding to the macrostructure of the composite (braid). In contrast, such surface strains were less prominent for the TBr_R beams in terms of magnitude and uniformity over the region, but nonetheless were greater as compared to the UBr₄₅ beam. As observed for the UBr beams, differences in the measured surface strains between TBr_R and UBr₄₅ beams correlated inversely with increased prevalence of localised crush under the loading roller.

The flexural strains recorded on the beam surface are shown in Figure 18. Compressive and tensile strains of increasing magnitude were observed in the top (strain 1) and bottom (strain 3) regions respectively for all the beams. TBr_A and UBr₆₀ beams showed approximately overlapping responses for each strain. Following onset of localised crushing in the TBr_R and UBr₄₅ beams, strain 1 measurements were unavailable due to the propagation of cracks into the RoI. This localised failure occurred earlier for the UBr₄₅ beam, showing a tendency towards localised crushing as compared to TBr_R beam. Similarly, curves corresponding to strain 2 and strain 3 also showed visible differences in magnitude but followed the same trend. As observed in Figure 17, strain-3, i.e. lower (tensile) region strains for the UBr₄₅ and TBr_R beams were greatly reduced as compared to the TBr_A and UBr₆₀ beams, again illustrating the tendency of the former (UBr₄₅ and TBr_R beams) towards localised crush failure rather than the global flexure deformation modes seen in the latter (TBr_A and UBr₆₀ beams).

Figure 19 shows the progression of section-wise y-displacements y₁, y₂ and y₃ with increasing crosshead displacement. Results for UBr beams had indicated that differences arising between the three discrete section-wise displacement analyses is positively correlated with localised crush. In order to quantify the disparity in region-wise displacements, the root mean square (RMS) difference between the mid and bottom region y-displacements was evaluated as per Equation 4.

$$\text{RMS}_{23} = \sqrt{\frac{\sum(y_2 - y_3)^2}{n}} \quad (4)$$

where RMS₂₃: root mean square difference between y₂ and y₃ and n: number of points on the sections.

The evolution of RMS_{23} with increasing crosshead displacement is shown in Figure 20. The data shown replicates the order observed for localised crush, thus showing a positive correlation between the two quantities.

The deformation analysis performed using both contact and optical strain measurement techniques revealed that the TBr_A beams experience a very similar deformation behaviour to that observed for the UBr_{60} beams. On the other hand, the TBr_R beams showed greater localised crushing as compared to TBr_A beams, but the TBr_R beam deformation was more inclined towards global flexure as compared to UBr_{45} beams. The superior performance of TBr_A beams over TBr_R beams shows the effectiveness of locally tailoring the fibre architecture across the entire thickness of the beam as compared to making an outer-layer modification globally along the beam.

Conclusions

This paper presents ‘tailor-braiding’ as a novel approach to create composite beams with higher structural efficiency than conventionally uni-braided beams. As such the performance of tailored braided beam structures with axial (TBr_A) and radial (TBr_R) braid angle variation was investigated in quasi-static three-point flexure. Based on the previously obtained flexure test results from uni-braided beams with angles of 45° and 60° (UBr_{45} and UBr_{60}), tailored beams with a step-wise $45^\circ/60^\circ/45^\circ$ axial braid angle configuration were manufactured using a start/stop braiding method. Beams with a globally-applied radial [$\pm 60^\circ/\pm 45^\circ/\pm 45^\circ$] variation (TBr_R) were also manufactured. The tailored (TBr_A , TBr_R) beams were tested in a static three-point flexure test and their mechanical performance and deformation behaviour were compared with UBr beams.

The TBr_A beams showed tow distortion (waviness) at the braid angle transition zone. Apart from the waviness, braid angle and thickness measurements in different regions of the TBr_A beams were in reasonable agreement with the corresponding measurements from UBr beams. It is proposed that a continuous braid angle transition (instead of step-wise) would minimise/eliminate the fibre waviness observed in this work that has arisen due to the step-transition in braid angle and start/stop nature of the manufacturing process. The performance indices of the TBr_A beams were higher than the UBr beams. Particularly interesting was the observation that despite being 24% lighter, the TBr_A beams showed statistically equivalent performance to the UBr_{60} , which had highest mechanical performance amongst the UBr beams. This superior performance of the TBr_A beams, despite the presence of fibre waviness, was encouraging and suggests that further improvements in performance might be achieved through elimination of defects. In spite of weighing the same as the TBr_A beams, the TBr_R beams did not offer any lightweighting benefit when utilised in this particular load case. Therefore, changing the braid angle in the loading region to 60° resulted in a replication of the deformation behaviour of UBr_{60} beams, while braiding the outer layer at 60° did not produce an equivalent change.

The results offer a demonstration of the lightweighting of potential of the proposed axial-wise tailor braiding (TBr_A) approach. It is proposed that future work varying the length of the central 60° region in TBr_A beams could optimise performance and yield further reduction in the weight of the beams without affecting deformation modes. Additionally, investigating structures produced with continuous braid angle transitions (as opposed to the step-wise discrete transition presented here), and investigating the effect of the same TBr_A approach in thermoset matrix-based composites would be worthwhile additions in this area of study.

Acknowledgements

The authors are thankful to the technical staff at WMG and Composite Braiding Limited for their time and support in this work.

Funding source

The author (Anubhav Singh) was funded through a WMG departmental scholarship.

Data Availability Statement

The raw/processed data required to reproduce these findings cannot be shared at this time as the data also forms part of an ongoing study.

References

- [1] Kyosev Y. Recent developments in braiding and narrow weaving. Berlin: Springer International Publishing; 2016.
- [2] Carey JP. Introduction to braided composites. In: Handbook of Advances in Braided Composite Materials. Woodhead Publishing; 2017, p. 1–21.
- [3] Slange TK. Rapid Manufacturing of Tailored Thermoplastic Composites by Automated Lay-up and Stamp Forming: A Study on the Consolidation Mechanisms. PhD Thesis, University of Twente. 2019.
- [4] High Performance Computing Studies: DOT HS 812 404. Department of Transportation. 2017.
- [5] Sturm R, Heieck F. Energy absorption capacity of braided frames under bending loads. *Compos Struct* 2015;134:957–65.
- [6] Harte AM, Fleck NA. On the mechanics of braided composites in tension. *Eur J Mech A/Solids* 2000;19:259–75.
- [7] Melenka GW, Carey JP. Development of a generalized analytical model for tubular braided-architecture composites. *J Compos Mater* 2017;51:3861–75.
- [8] Falzon PJ, Herszberg I. Mechanical performance of 2-D braided carbon/epoxy composites. *Compos Sci Technol* 1998;58:253–65.
- [9] Potluri P, Manan A, Francke M, Day RJ. Flexural and torsional behaviour of biaxial and triaxial braided composite structures. *Compos Struct* 2006;75:377–86.
- [10] Priem C, Othman R, Rozycki P, Guillon D. Experimental investigation of the crash energy absorption of 2.5D-braided thermoplastic composite tubes. *Compos Struct* 2014;116:814–26.
- [11] Gautam M, Potluri P, Ogini S, Jain P. Necking behaviour of flattened tubular braided composites. In: ICCM 2015: Proceedings of the 20th International Conference on Composite Materials, Copenhagen, July 2015.
- [12] Fujihara K, Yoshida E, Nakai A, Ramakrishna S, Hamada H. Influence of micro-structures on bending properties of braided laminated composites. *Compos Sci Technol* 2007;67:2191–8.
- [13] Tate JS, Kelkar AD. Flexural behavior of biaxial braided composites. In: Proceedings of ASME International Mechanical Engineering Congress and Exposition, Orlando, November 2005.
- [14] Laberge-Lebel L, Van Hoa S. Manufacturing of braided thermoplastic composites with carbon/nylon commingled fibers. *J Compos Mater* 2007;41:1101–21.
- [15] Carey J, Fahim A, Munro M. Design of braided composite cardiovascular catheters based on required axial, flexural, and torsional rigidities. *J Biomed Mater Res Part B Appl Biomater An Off J Soc Biomater Japanese Soc Biomater Aust Soc Biomater Korean Soc Biomater* 2004;70:73–81.
- [16] Fujihara K, Teo K, Gopal R, Loh PL, Ganesh VK, Ramakrishna S, et al. Fibrous composite materials in dentistry and orthopaedics: review and applications. *Compos Sci Technol* 2004;64:775–88.
- [17] Boss JN, Ganesh VK. Fabrication and properties of graded composite rods for biomedical applications. *Compos Struct* 2006;74:289–93.
- [18] Ganesh VK, Choo TS. Modulus graded composite adherends for single-lap bonded joints. *J Compos Mater* 2002;36:1757–67.
- [19] Stanier D, Gent I, Roy SS, Hamerton I, Potluri P, Ivanov DS. Mechanical behaviour of patterned multi-matrix composites with gradient properties. In: ECCM 2016: Proceedings of the 17th European Conference on Composite Materials, Munich, June 2016.
- [20] Stanier D, Radhakrishnan A, Gent I, Roy SS, Hamerton I, Potluri P, et al. Matrix-graded and fibre-steered composites to tackle stress concentrations. *Compos Struct* 2019;207:72–80.
- [21] Huang Z-M, Wang Q, Ramakrishna S. Tensile behaviour of functionally graded braided carbon fibre/epoxy composite material. *Polym Polym Compos* 2002;10:307–14.

- [22] Duan L, Xiao N, Li G, Xu F, Chen T, Cheng A. Bending analysis and design optimisation of tailor-rolled blank thin-walled structures with top-hat sections. *Int J Crashworthiness* 2017;22:227–42.
- [23] Sun G, Pang T, Zheng G, Song J, Li Q. On energy absorption of functionally graded tubes under transverse loading. *Int J Mech Sci* 2016;115–116:465–80.
- [24] Keating EM. Lightweighting of Stiffness Critical Advanced High Strength Steel Structures using Fibre Reinforced Plastics. PhD Thesis. University of Warwick, 2016.
- [25] Sun G, Yu H, Wang Z, Xiao Z, Li Q. Energy absorption mechanics and design optimization of CFRP/aluminium hybrid structures for transverse loading. *Int J Mech Sci* 2019;150:767–83.
- [26] Singh A, Reynolds N, Keating E, Barnett A, Barbour S, Hughes DJ. The effect of braid angle on the flexural performance of structural braided thermoplastic composite beams. *Compos Struct* 2020:113314.
- [27] Wu Z, Shen Y, Pan Z, Hu X. Three-point Bending Behavior and Energy Absorption Capacity of Composite Tube Reinforced by Gradient Braided Structure in Radial Direction. *Fibers Polym* 2019;20:1455–66.
- [28] Nishimoto H, Ohtani A, Nakai A, Hamada H. Prediction Method for Temporal Change in Fiber Orientation on Cylindrical Braided Preforms. *Text Res J* 2010;80:814–21.
- [29] Singh A, Reynolds N, Carnegie CR, Micallef C, Keating EM, Winnett J, Barnett AE, Barbour SK, Hughes DJ. A novel route for volume manufacturing of hollow braided composite beam structures. *Adv Manuf Polym Compos Sci* 2019:1–6.
- [30] Tukey JW. The collected works of John W. Tukey. vol. 1. Taylor & Francis; 1984.

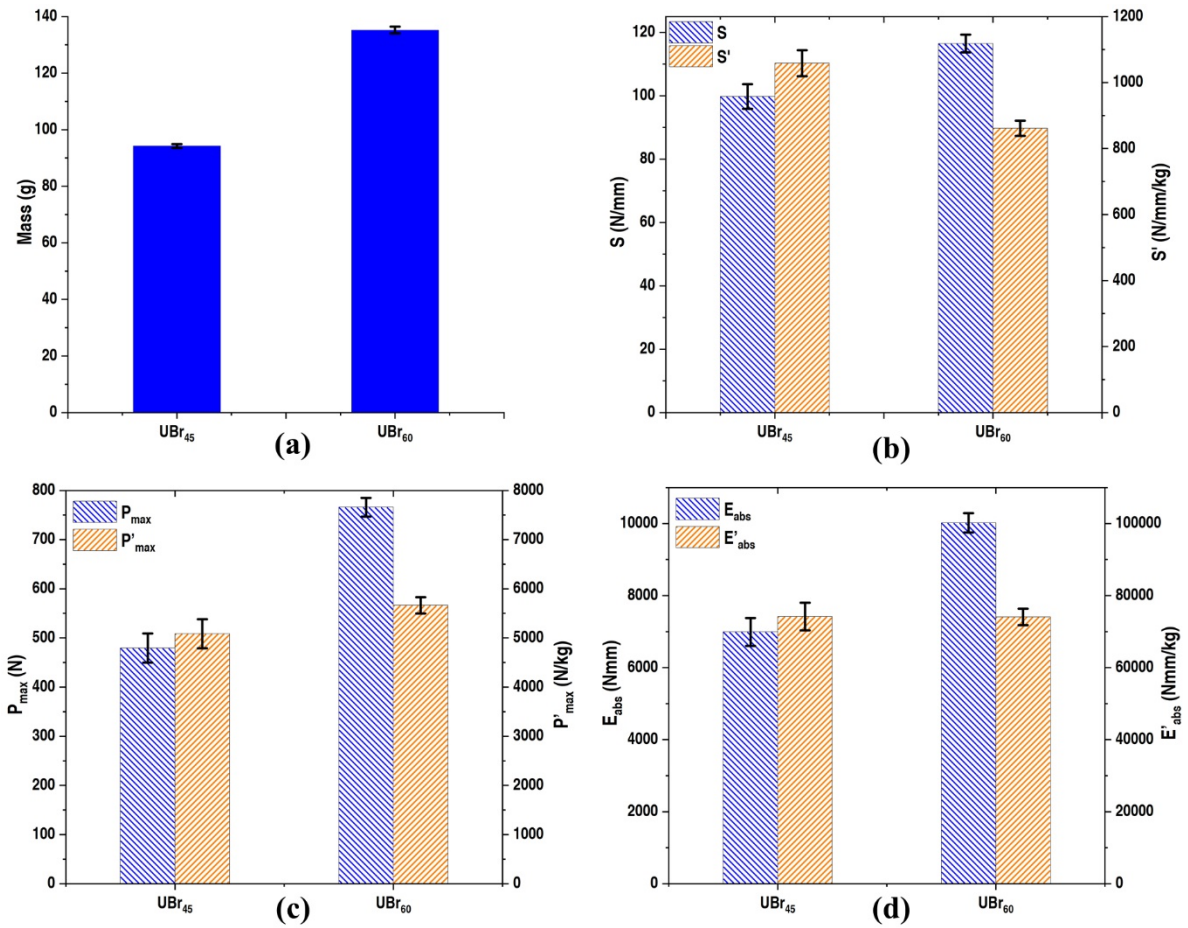


Figure 1 Measured values of (a) mass; (b) S and S'; (c) P_{max} and P' _{max} and (d) E_{abs} and E' _{abs} of the UBr beams. Note: bars represent mean values from 6 repeats and errors represent one standard deviation

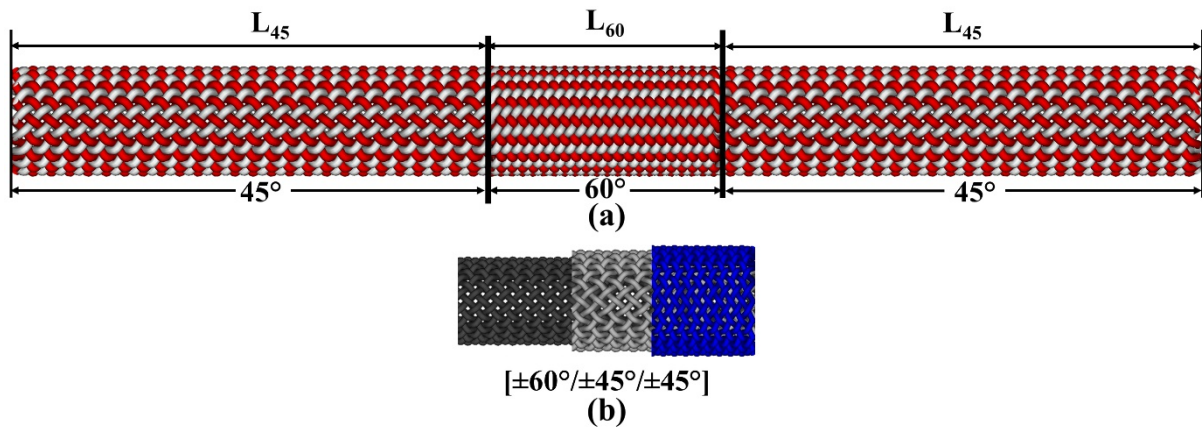


Figure 2 Schematic of axial (a) and radial (b) braid angle variation. Note: L₄₅ and L₆₀ represent the lengths of 45° and 60° regions respectively

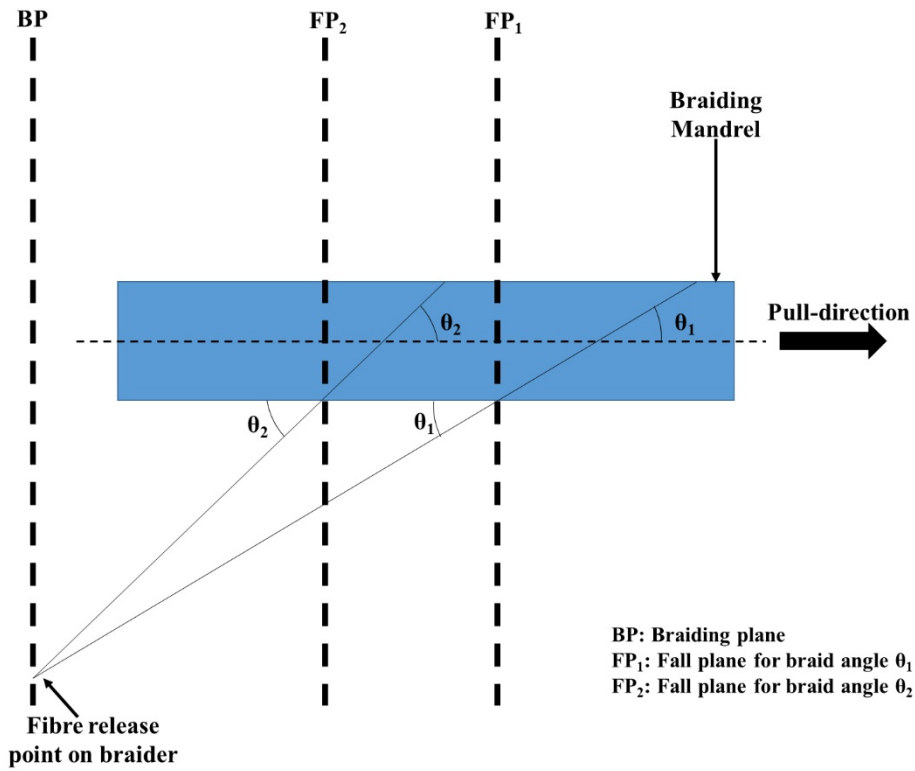


Figure 3 Schematic of the braiding process showing the location of fall planes corresponding to different braid angles

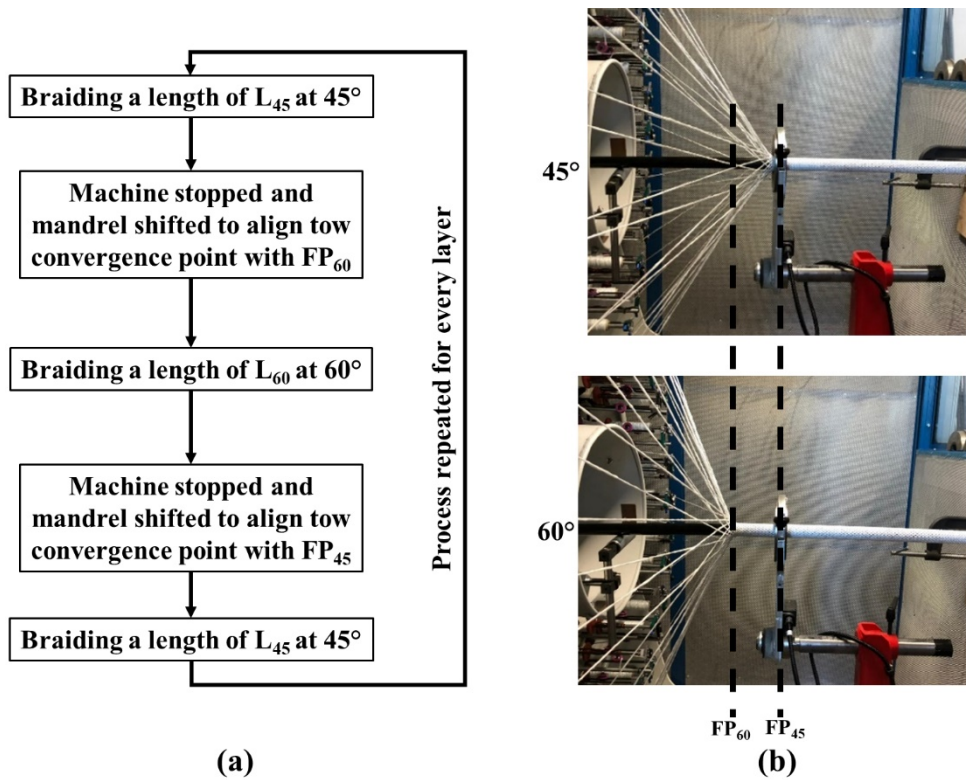


Figure 4 Start-stop braiding: (a) Steps for adjustment in braid angle and (b) Fall planes for 45° and 60° on the braiding mandrel

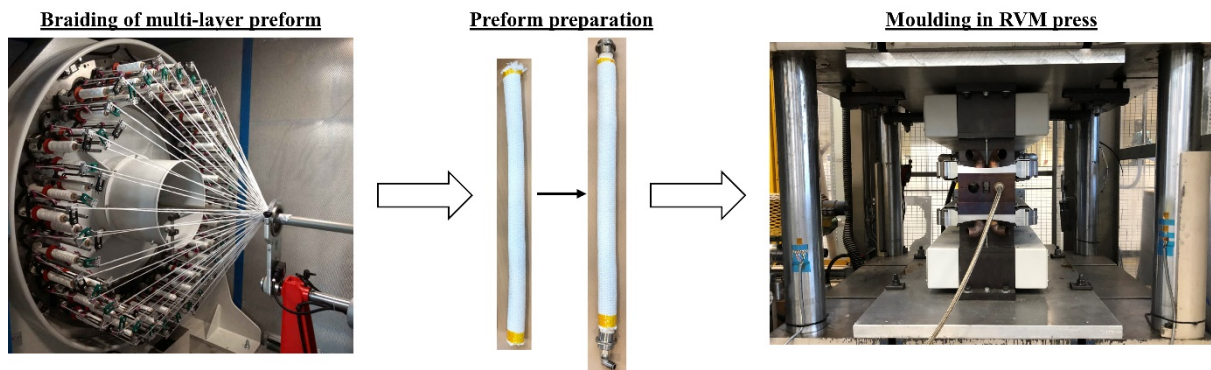


Figure 5 Steps involved in manufacturing of the braided beams (left: Braiding onto mandrel, centre: preform preparation for RVM and right: preform inside closed press with connected pressure line during RVM)

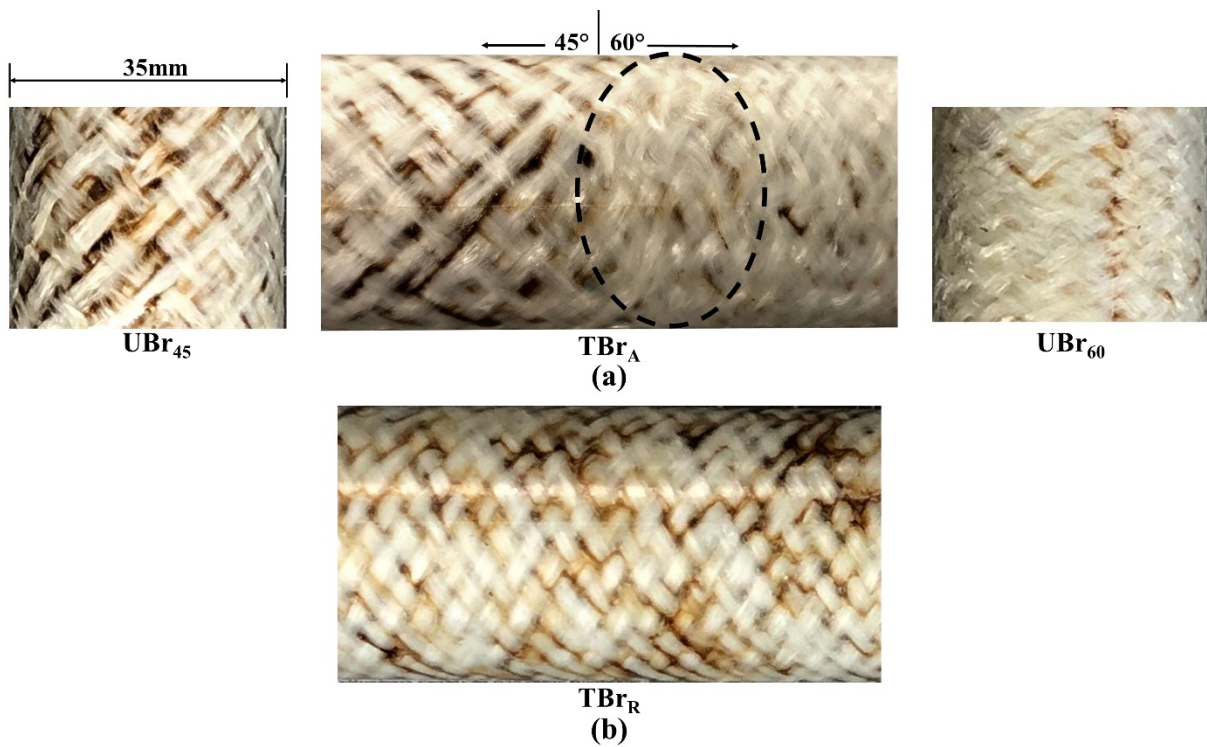


Figure 6 Outer surfaces of (a) TBr_A and UBr beams; (b) TBr_R. Note: encircled region shows fibre waviness in TBr_A beams

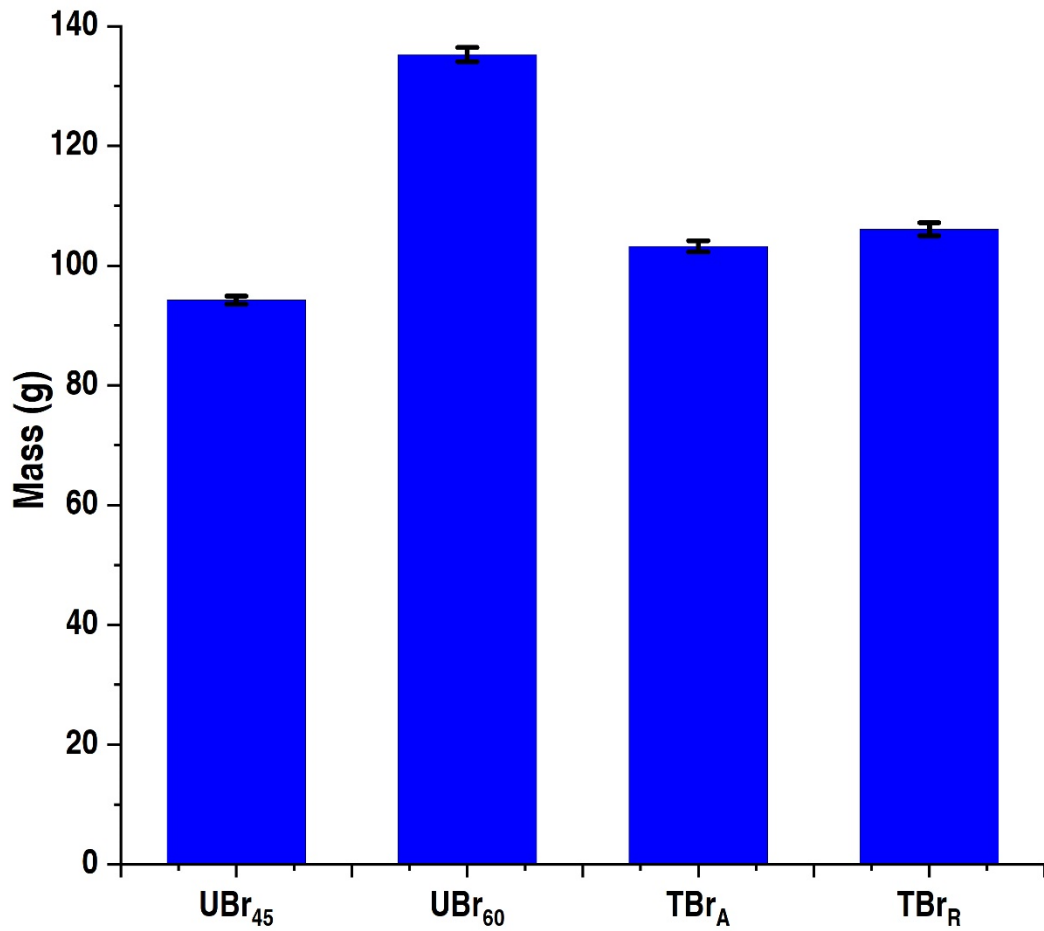


Figure 7 Measured mass of the UBr and TBr beams. Note: bars represent mean values from all repeats and errors represent one standard deviation

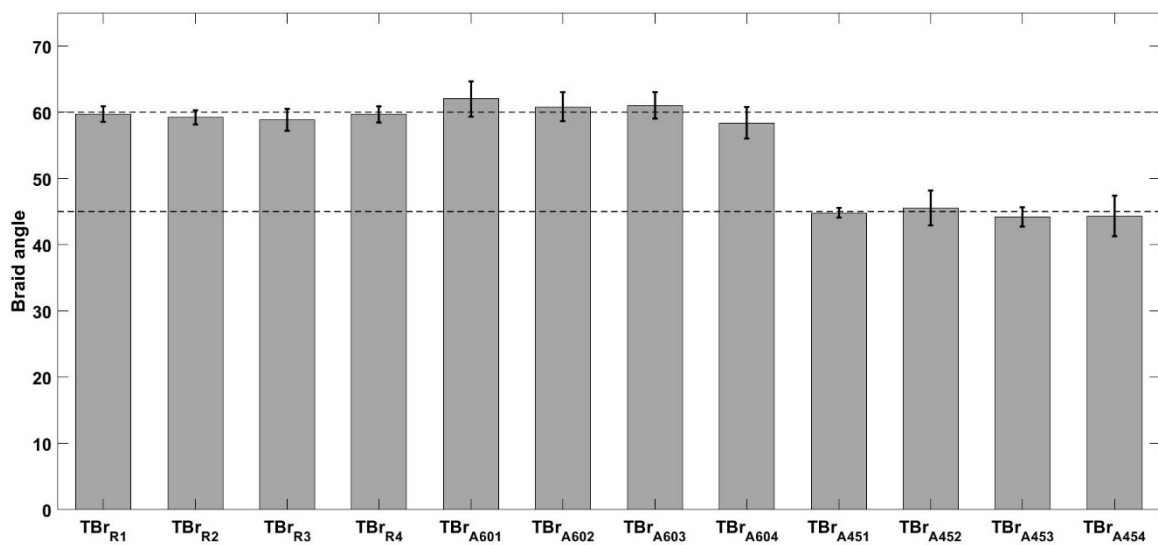


Figure 8 Measured braid angle for TBr beams. Note: bars represent mean values from all repeats and errors represent one standard deviation

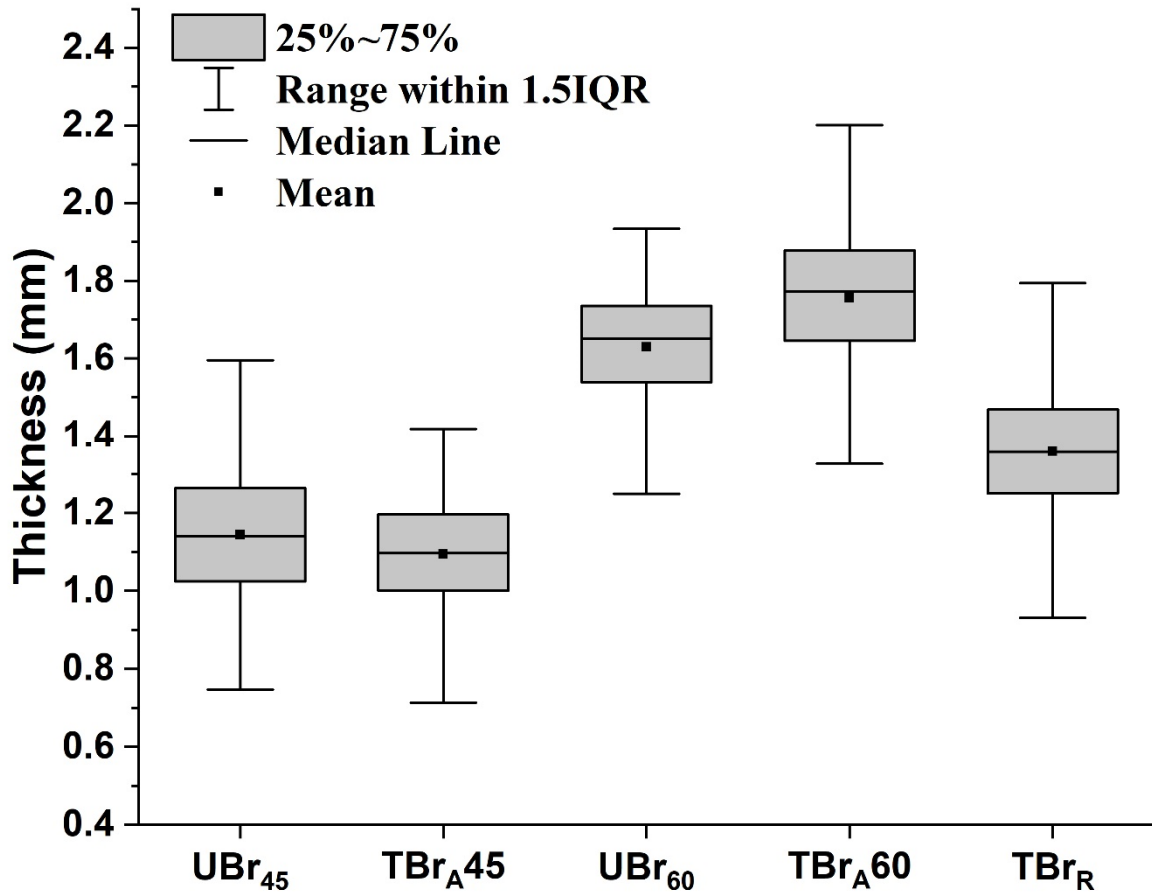


Figure 9 Box plots representing thickness distributions corresponding to TBr beams. Note: thickness distributions of UBr beams are shown for comparison. Note: IQR represents Inter Quartile Range

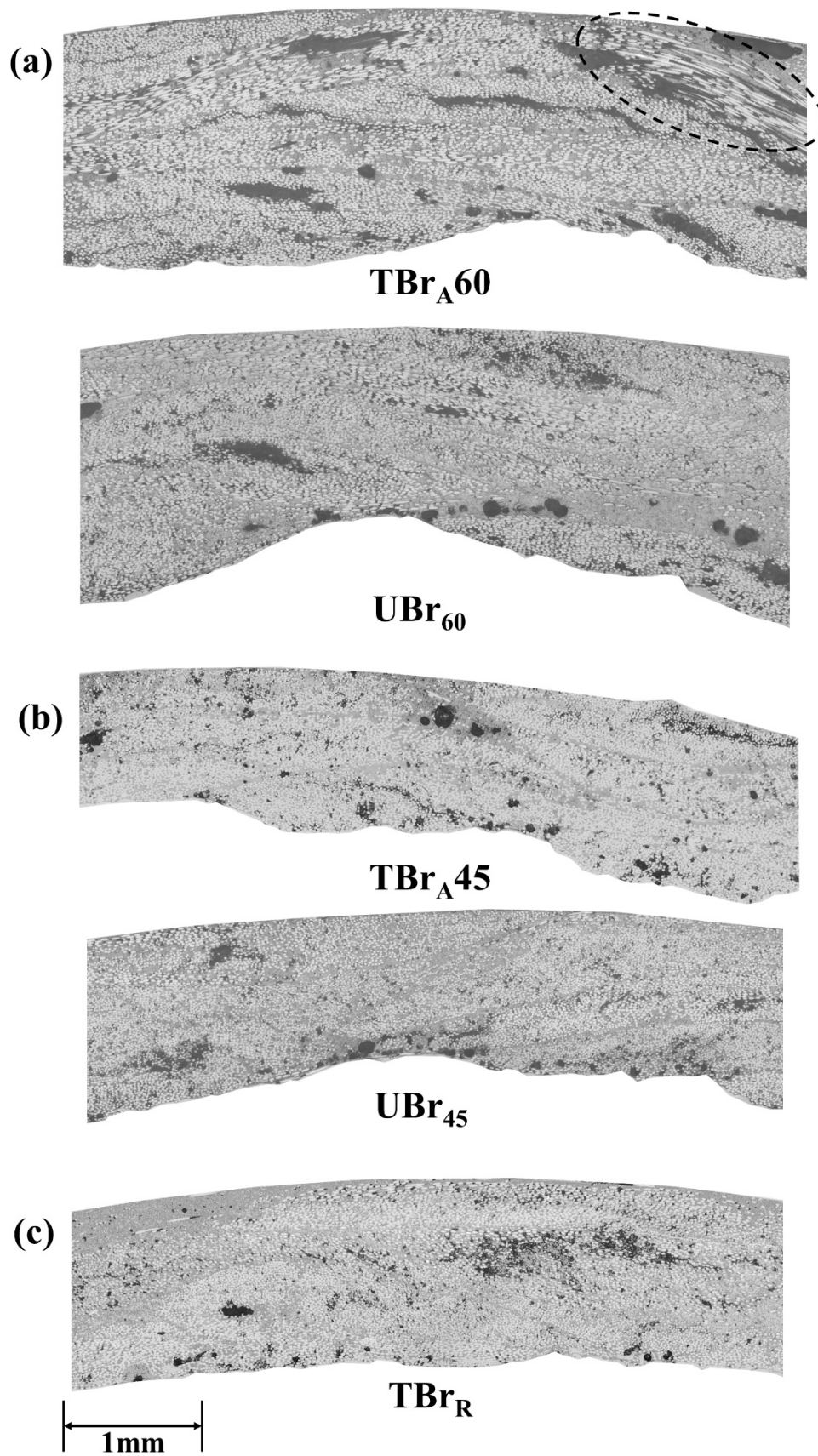
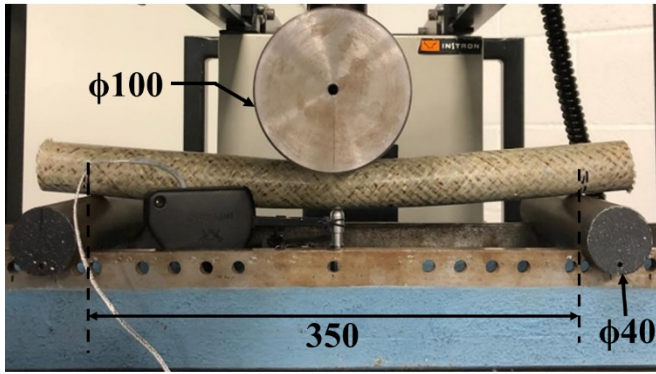


Figure 10 Micrographs of braided beam sections corresponding to (a) 60° region of TBr_A beam with highlighted fibre waviness; (b) 45° region of TBr_A beam; (c) TBr_R beam. Note: Micrographs of UBr beam sections are also shown for comparison

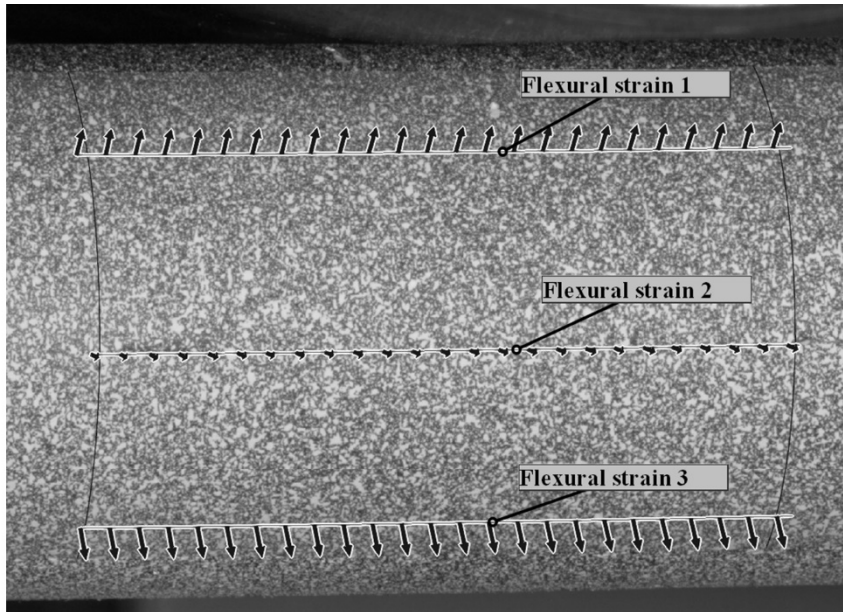


(a)

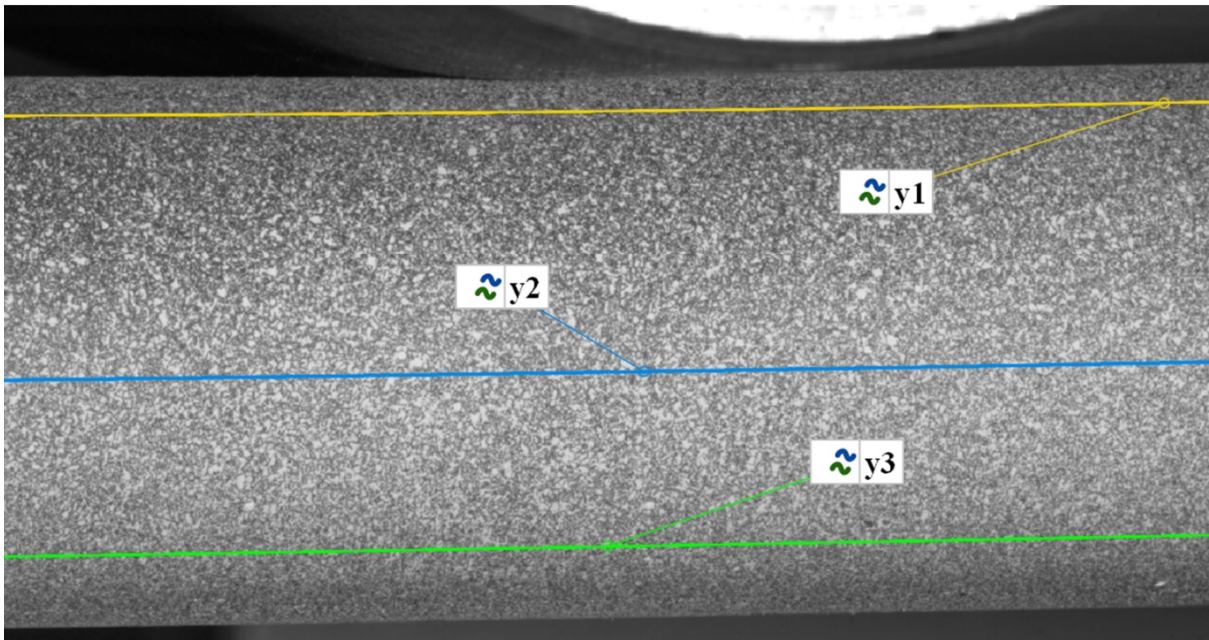


(b)

Figure 11 (a) Three-point flexure setup on the test machine frame and (b) deflectometer assembly. Note: all measurements in mm (Taken from [26])

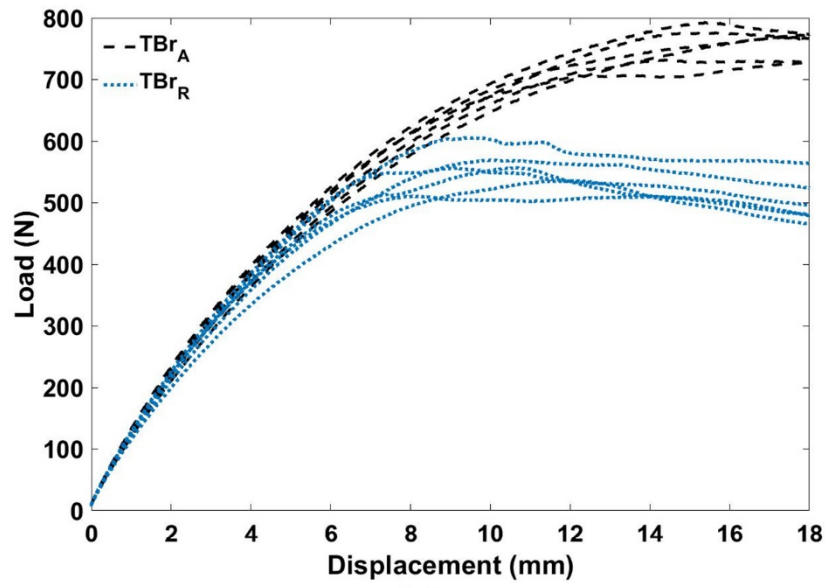


(a)

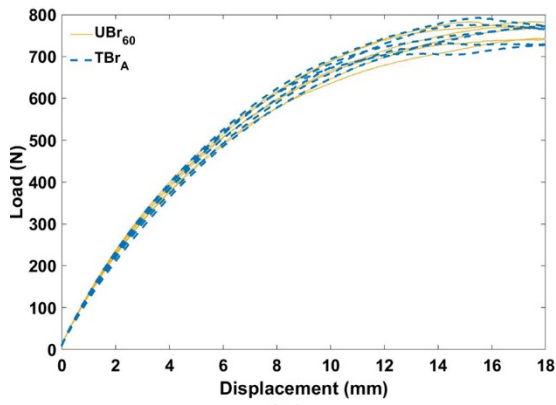


(b)

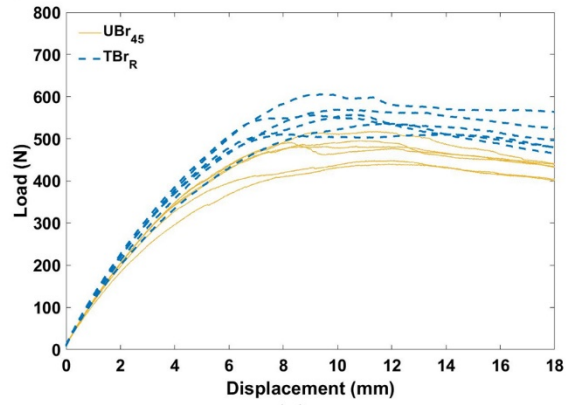
Figure 12 Horizontal sections constructed on the surface of beam in GOM Correlate for evaluating (a) flexural strains; (b) vertical displacements



(a)



(b)



(c)

Figure 13 Load-displacement data from three-point flexure experiments of (a) all tailor-braided beams; (b) TBr_A and UBr₆₀ beams; (c) TBr_R and UBr₄₅ beams

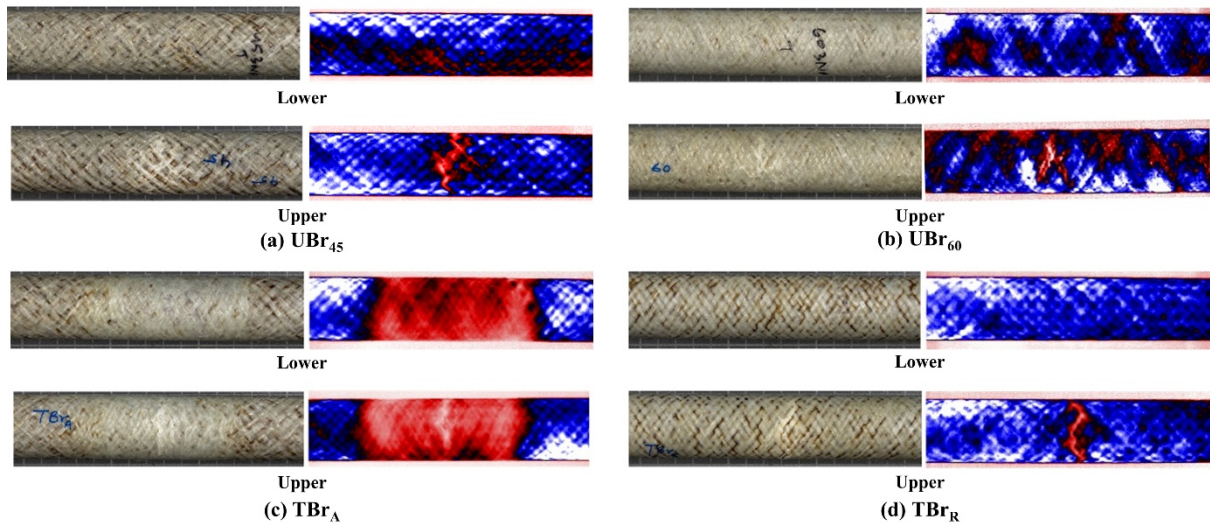


Figure 14 Optical and thermal images corresponding to upper and lower surfaces of (a) UBr₄₅, (b) UBr₆₀, (c) TBr_A and (d) TBr_R beams. Note: Colour levels individually adjusted for each beam type and do not represent a common temperature scale

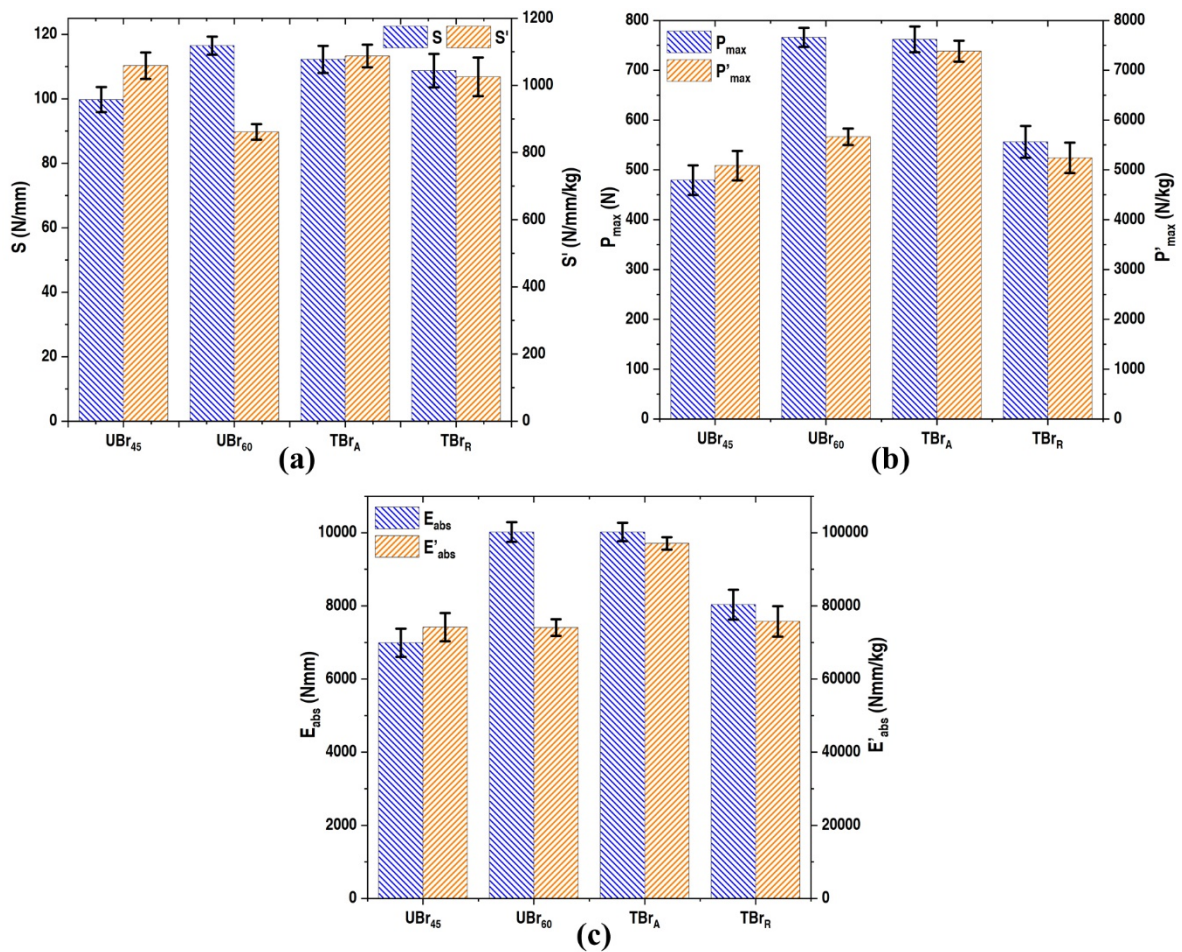


Figure 15 Measured mean values of (a) S and S' ; (b) P_{\max} and P'_{\max} and (c) E_{abs} and E'_{abs} of the UBr and TBr beams. Note: bars represent mean values from all repeats and errors represent one standard deviation

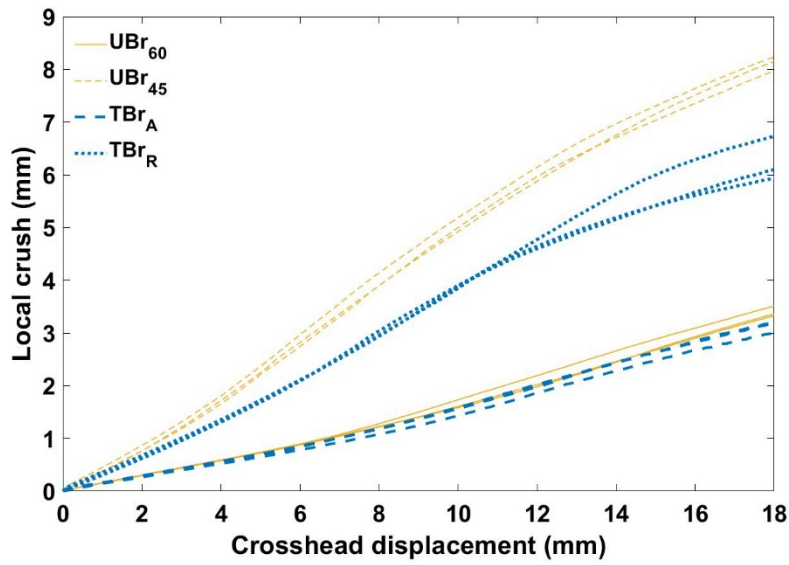


Figure 16 Progression of localised crushing during three-point flexure

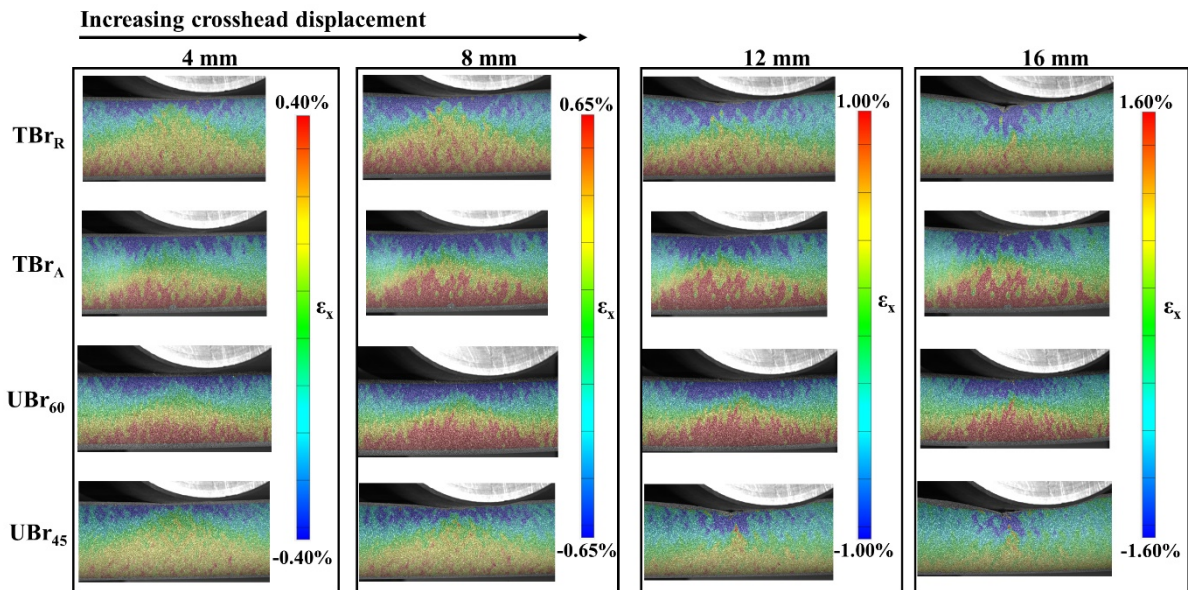


Figure 17 Progression of axial surface strain from 3D DIC data with crosshead displacement during three-point flexure

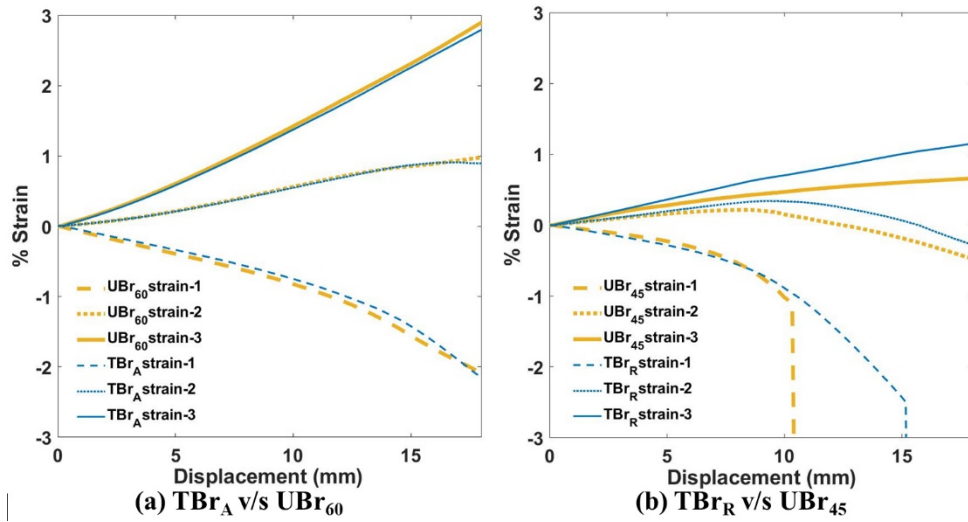


Figure 18 Comparison of region-wise flexural strain evolution between (a) TBr_A and UBr₄₅ and (b) TBr_R and UBr₄₅ beams

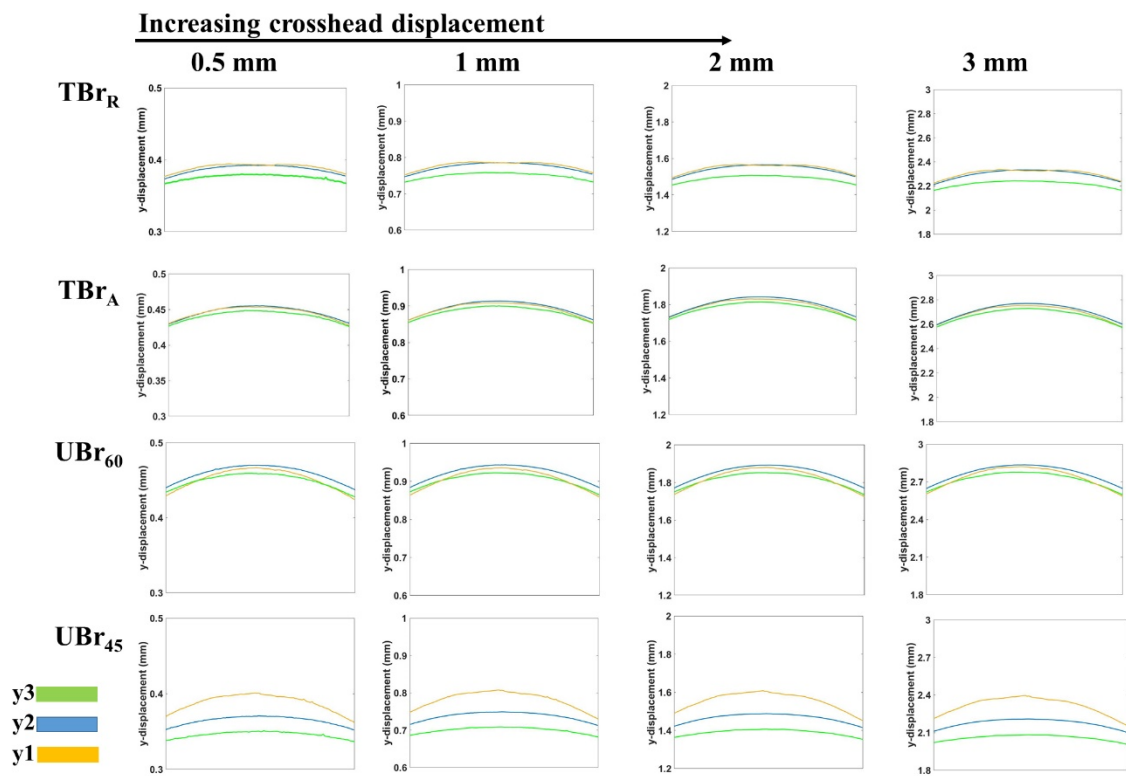


Figure 19 Evolution of downward y-displacement y1, y2 and y3 for TBr and UBr beams with increasing crosshead displacement during three-point flexure

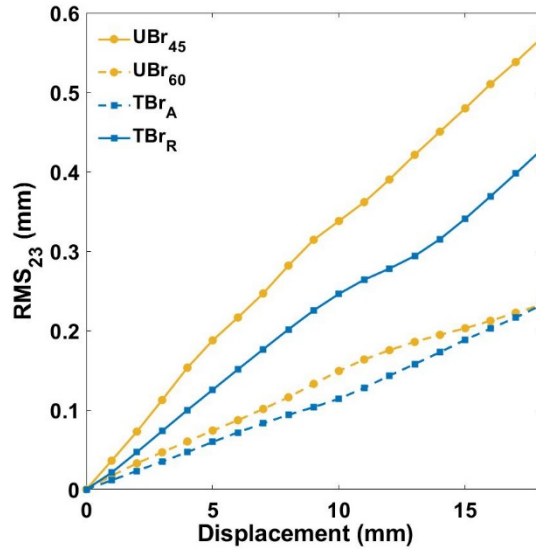


Figure 20 Evolution of RMS difference between mid-region and bottom-region y-displacements during three-point flexure

Table 1 p-values obtained from ANOVA performed for comparing the mechanical performance of UBr₄₅ and UBr₆₀ beams

Property	p-value
Specific Stiffness	8.99E-07
Specific Peak load	0.002
Specific Energy Absorption	0.962

Table 2 Properties of commingled E-glass/PA6 material and braiding parameters

Commingled material			Braiding process		
Linear weight	1650 g/km	PA6 density	1.15 g/cm ³	Number of carriers	32
Fibre volume fraction	54%	PA6 melting point	221 °C	Braid architecture	1×1
E-glass density	2.54 g/cm ³	PA6 glass transition temperature	60 °C	Number of braided layers	3

Table 3 Three-point flexure testing parameters

Parameter	
Beam length	420 mm
Support span	350 mm
Support roller diameter	40 mm
Loading roller diameter	100 mm
Crosshead displacement rate	10 mm/min
Preload	10 N
Machine compliance induced error	~0.03mm
Load cell error	~2%

Table 4 DIC system parameters employed during image acquisition and analysis

Parameter	
Sensor	GOM 12M with Titanar 100 mm lens
Image window	4000 pixel × 3000 pixel
Measurement area	150 mm × 100 mm
Calibration plate used	CP20 90 × 72
Facet size	19 pixels (16 pixels step size)
Depth of field	39 mm
Frame rate	2 Hz

Table 5 Mean bias and precision of DIC measurements estimated from static images

Mean bias	Mean precision	Mean bias	Mean precision	Mean bias	Mean precision
[ϵ_x (%)]	[ϵ_x (%)]	[dx (mm)]	[dx (mm)]	[dy (mm)]	[dy (mm)]
-0.0004	0.0175	0.0023	0.0004	-0.0001	0.0005

Table 6 p-values obtained from ANOVA performed for comparing the mechanical performance of TBr and UBr beams

Property	p-value
Specific Stiffness	1.93E-08
Specific Peak Load	1.81E-12
Specific Energy Absorption	4.33E-11

Table 7 q-values obtained from Tukey-Kramer post-hoc analysis performed for TBr and UBr beams. Note: values indicating a statistically significant difference are highlighted in **bold**

Pair	q(S')	q(P' _{max})	q(E' _{abs})	q _{critical}
UBr ₄₅ -UBr ₆₀	12.01	5.66	0.07	4.00
TBr _A -TBr _R	3.76	20.94	16.52	4.00
UBr ₄₅ - TBr _A	1.74	22.48	17.74	4.00
UBr ₄₅ -TBr _R	2.02	1.54	1.22	4.00
UBr ₆₀ - TBr _A	13.76	16.82	17.81	4.00
UBr ₆₀ -TBr _R	10.00	4.12	1.29	4.00